Canadian Science Publishing

ARTICLE

Development of a poly-axial platen for testing true-triaxial behavior of rocks

Prasoon Garg, Bhardwaj Pandit, Brijes Mishra, and G.L. Sivakumar Babu

Can. Geotech. J. Downloaded from cdnsciencepub.com by Indian Institute of Science Bengaluru (IISc) on 01/03/22
For personal use only.

Abstract: Mining at greater depths can lead to stress-induced failure, especially in areas of high horizontal in situ stress. The induced stresses around the opening are known to be in a poly-axial stress state where, $\sigma_1 \neq \sigma_2 \neq \sigma_3$ with special case of $\sigma_3 = 0$ and $\sigma_1, \sigma_2 \neq 0$ at its boundary, where σ_1, σ_2, σ_3 are major, intermediate, minor principal stress, respectively. The conventional triaxial testing does not represent the actual in situ strength of the rock in regions of high horizontal stress, as it ignores the influence of intermediate principal stress (σ_2). The typical poly-axial testing (biaxial and true-triaxial tests) of intact rock mostly requires sophisticated and expensive loading systems. This study investigated the mechanical behavior of intact rock under a poly-axial stress state using a simple and cost-effective design. The apparatus consists of a biaxial frame and a confining device. The biaxial frame has two platens that apply equal stress in both directions ($\sigma_1 = \sigma_2$) on a 50.8 mm cubical specimen when placed inside the uniaxial loading device. The confining device performed separate biaxial tests under constant intermediate principal stress (σ_2 = constant) and true-triaxial tests when used along with the biaxial frame. This study then compared the failure modes and peak strength of Berea sandstone specimens with other biaxial–triaxial devices to validate the design of the poly-axial apparatus. We also performed uniaxial tests on both standard cylindrical samples and prismatic specimens of different slenderness ratios. These tests provided a complete understanding of the failure mode transition from standard uniaxial compressive tests to triaxial stress conditions on cubical specimens. Additionally, this study determined best-fitted strength envelopes for biaxial and triaxial stress state. Based on regression analysis, we found a quadratic polynomial to be a good fit to biaxial strength envelope. For the true-triaxial strength envelope, we found the three-dimensional (3D) failure criterion to be a good fit with R^2 of 0.964.

Key words: poly-axial testing, biaxial frame, stress paths, failure modes, true-triaxial tests, intermediate principal stress, Berea sandstone, biaxial platens.

Résumé : L'exploitation minière à de plus grandes profondeurs peut conduire à une défaillance induite par les contraintes, en particulier dans les zones de fortes contraintes horizontales in situ. Les contraintes induites autour de l'ouverture sont connues pour être dans un état de contrainte poly-axiale où, $\sigma_1 \neq \sigma_2 \neq \sigma_3$ avec le cas particulier de $\sigma_3 = 0$ et $\sigma_1, \sigma_2 \neq 0$ à sa limite, où σ_1, σ_2, σ_3 sont la contrainte principale majeure, intermédiaire, mineure, respectivement. L'essai triaxial conventionnel ne représente pas la résistance in situ réelle de la roche dans les régions à forte contrainte horizontale, car il ignore l'influence de la contrainte principale intermédiaire (σ_2). Les essais poly-axiaux typiques (essais biaxiaux et triaxiaux réels) sur des roches intactes nécessitent généralement des systèmes de chargement sophistiqués et coûteux. Cette étude a examiné le comportement mécanique de la roche intacte sous un état de contrainte poly-axiale en utilisant une conception simple et rentable. L'appareil se compose d'un cadre biaxial et d'un dispositif de confinement. Le cadre biaxial comporte deux plateaux qui appliquent une contrainte égale dans les deux directions ($\sigma_1 = \sigma_2$) sur un échantillon cubique de 50,8 mm lorsqu'il est placé dans le dispositif de chargement uniaxial. Le dispositif de confinement a effectué des essais biaxiaux séparés sous contrainte principale intermédiaire constante (σ_2 = constante) et des essais triaxiaux réels lorsqu'il a été utilisé avec le cadre biaxial. Cette étude a alors comparé les modes de défaillance et la résistance maximale des spécimens de grès de Berea avec d'autres dispositifs biaxiaux–triaxiaux afin de valider la conception de l'appareil poly-axial. Nous avons également effectué des essais uniaxiaux sur des échantillons cylindriques standard et des échantillons prismatiques de différents rapports d'élancement. Ces essais ont permis une compréhension complète de la transition du mode de défaillance entre les essais de compression uniaxiale standard et les conditions de contrainte triaxiale sur des échantillons cubiques. En outre, cette étude a déterminé les enveloppes de résistance les mieux ajustées pour les états de contrainte biaxiale et triaxiale. Sur la base de l'analyse de régression, nous avons constaté qu'un polynôme quadratique correspondait bien à l'enveloppe de résistance biaxiale. Pour l'enveloppe de résistance triaxiale réelle, nous avons trouvé que le critère de rupture tridimensionnelle (3D) était un bon ajustement avec un R^2 de 0,964. [Traduit par la Rédaction]

Mots-clés : essais poly-axiaux, cadre biaxial, chemin de contrainte, modes de défaillance, essais triaxiaux réels, contrainte principale intermédiaire, grès de Berea, plateaux biaxiaux.

Received 21 June 2020. Accepted 1 February 2021.

P. Garg. Department of Civil and Environmental Engineering, Colorado School of Mines, Golden, CO, USA.
B. Pandit and G.L. Sivakumar Babu. Department of Civil Engineering, Indian Institute of Science, Bangalore, India.
B. Mishra. Department of Mining Engineering, West Virginia University, Morgantown, WV, USA.

Corresponding author: Brijes Mishra (email: brijes.mishra@mail.wvu.edu).
© 2021 The Author(s). Permission for reuse (free in most cases) can be obtained from copyright.com.

Can. Geotech. J. Downloaded from cdnsciencepub.com by Indian Institute of Science Bengaluru (IISc) on 01/03/22
For personal use only.

1. Introduction

Excavation at deeper depths often creates adverse stress conditions around an underground mine opening. In addition to in situ stresses, the excavated opening produces induced stresses that may initiate failure of the rock mass. Three mutually perpendicular principal stresses ($\sigma_1 > \sigma_2 > \sigma_3$, where σ_1, σ_2, σ_3 are major, intermediate, minor principal stress, respectively) can represent the stress state in the Earth, which is usually in a poly-axial state. However, on the boundary of an unsupported excavation, a biaxial stress state exists where $\sigma_3 = 0$ and σ_1, $\sigma_2 \neq 0$. In addition, the minimum principal stress is smaller when compared to the other two stresses in the region (within the pressure arch) around the vicinity of the opening (Cai 2008). Such planar stresses often dictate the constitutive behavior of rock mass around an opening, especially in regions of high horizontal stress such as the Central Appalachian region containing the eastern USA coalfields. According to a study by Mark and Barczak (2000), the eastern USA has a major horizontal stress two to three times that of the vertical stress, while the minor horizontal stress is approximately equal to the vertical stress. These stress conditions often result in various ground control problems, such as buckling, cutter failure, spalling, and rockbursts (Smith 1963; Bétournay and Mitri 2003; Mitri et al. 2005). The two most commonly used criteria in the design of underground structures, Mohr–Coulomb and Hoek–Brown, do not account for the influence of intermediate principal stress σ_2, as they only consider σ_1 and σ_3, making them unsuitable in cases of planar loading. For instance, these criteria cannot explain the cause of strainbursts in deep mine openings or zones of high compressive stresses that result in spalling of thin slabs of rock roughly parallel to the free face of opening (Bétournay and Mitri 2003). Therefore, a generalized failure criterion that accounts for the influence of intermediate principal stress is essential for rocks.

Various researchers have comprehensively investigated the influence of the intermediate principal stress on rock behavior (Handin et al. 1967; Colmenares and Zoback 2002; Al-Ajmi and Zimmerman 2005). Several failure criteria have included the intermediate principal stress to describe rock strength under true-triaxial stress states, such as the modified Wiebols and Cook (1968) criterion and Mogi (1971) criterion. However, no singular, specific criterion was found to fit most types of rock. For instance, Colmenares and Zoback (2002) found that out of seven different failure criteria, only the modified Lade criterion fit the failure data of Dunham dolomite and Solenhofen limestone. Initially, Hobbs (1962) performed biaxial tests on hollow cylinders of coal (Hobbs 1962). Subsequently, biaxial laboratory tests used the cubical specimen (Brown 1974; Amadei et al. 1984; Mitri et al. 2005). However, these studies used true-triaxial or biaxial devices that are quite sophisticated and required time-consuming efforts (Amadei et al. 1984; Haimson and Chang 2000; Kulatilake et al. 2006; Walsri et al. 2009; Yun et al. 2010). Therefore, the current study designs a simple and cost-effective poly-axial apparatus that can be used easily with a uniaxial loading device. This apparatus is an improved version of the biaxial device by Arora and Mishra (2015).

This study investigates the mechanical behavior of intact rock under a poly-axial stress state. The study's objective was to design a simple and cost-effective apparatus which, when placed under a uniaxial loading machine, would mimic the biaxial and true-triaxial load conditions. This apparatus consists of a biaxial frame and a confining device. The biaxial device is an improved version of the device by Arora and Mishra (2015), consisting of two platens that apply equal stresses on a 2 in (1 in = 25.4 mm) cubical specimen when placed inside a uniaxial compressive loading device. The confining device applied a constant confinement on the specimen and operated along with a biaxial frame to represent triaxial stress conditions. To validate the design of the poly-axial apparatus, we compared the change in failure modes and peak strength of Berea sandstone samples from uniaxial to triaxial stress conditions with standard triaxial–biaxial devices. Furthermore, this study also analyzes the influence of specimen size on the failure mode of Berea sandstone to gain a complete understanding of the failure mode transition from standard uniaxial compressive strength (UCS) test to triaxial test on cubical specimen.

2. Experimental design

The design of biaxial frame was based on the device by Arora and Mishra (2015) (Fig. 1*a*). The original frame consists of two mild hardened steel platens with arms (extended section of the platen) mounted on a 50.8 mm (2 in.) cubical rock specimen. The arms have four surface areas ("e", "f", "g", and "h") that apply equal load onto four faces of the cubical specimen. Two arms (one of each platen, "g" and "h") are 50.8 mm (2 in.) in length, while the remaining two arms ("e" and "f") are slightly shorter in length at 45.7 mm (1.8 in.) to ensure that the two platens are not in contact during the loading (Fig. 1*a*). This study assumes that the adjacent arms of each platen will apply an equal load to the specimen, replicating the biaxial stress conditions with $\sigma_1 = \sigma_2$ and $\sigma_3 = 0$. However, numerical analysis in 3DEC indicated an unsymmetrical displacement profile in the specimen (Fig. 1*b*) that would produce rotation at one side of the specimen. Therefore, we redesigned the frame to include symmetrical arms (Fig. 2) to overcome these limitations. The improved design, when simulated in 3DEC, showed symmetric vertical displacement contour without any rotation (Fig. 1*c*). The inner surfaces of the two platens were ground smooth to ensure that there are no stress concentrations due to any surface undulations.

The biaxial frame (Fig. 2) can apply only one set of biaxial stress ($\sigma_1 = \sigma_2$). Therefore, this study performed biaxial tests with constant intermediate principal stress σ_2 using a confining device (controlled with hydraulic jack) along with two steel cubical spacers (Fig. 3*a*). The confining device consists of two square plates with the dimensions of 49.53 mm (length) × 49.53 mm (breadth) × 6.35 mm (height). The square plates attach to the two hollow beams that interconnect through tension rods. The device suspends the beams through the mounting plate attached to the upper platen of the load frame using ball joint rods. The setup connects to the plunger of a hydraulic jack, which attaches to the hydraulic ram on the left side. The hydraulic jack controlled the confinement stress on the specimen during the biaxial test. The device has two cubical steel spacers (dimensions of 50.8 mm × 50.8 mm × 49.53 mm) on the top and bottom of the specimen; these spacers transfer the axial load from the platens of the uniaxial loading frame to the specimen, whereas the square plates of the confining device applied constant intermediate stress. Additionally, this study performed true-triaxial tests using a combination of the biaxial frame and special device (Fig. 3*b*). We placed the entire setup inside of the compression-testing machine (Fig. 3*b*) to replicate novel triaxial loading condition (Ma et al. 2017), i.e., $\sigma_1 = \sigma_2 > \sigma_3$ and σ_3 = constant. It is important to note that there is a limit to the amount of load that the square plates of the confining device can apply. This limit depends on the tensile strength of tension rods and other joints, which attach these rods to the hollow beams. Moreover, indentation loading on the beam will occur at the screw joint location, which is another limiting factor.

A fiberboard sheet of 1 mm thickness (Lundborg 1967) between the rock and platen minimized the shear stress along the interface for all tests; this sheet also ensured that the applied load to the rock was close to the true-biaxial and -triaxial state along with uniform stress distribution in an irregular ended specimen. In uniaxial tests, we placed the cubical steel spacers at the top and bottom of the specimen. This placement ensured uniform

Fig. 1. (*a*) Platen designed by Arora and Mishra (2015); vertical displacement contours: (*b*) biaxial device by Arora and Mishra (2015) and (*c*) modified biaxial design used in this study. (All dimensions in inches (1 in. = 25.4 mm).) Nb, bottom notch; Nu, upper notch. [Color online.]

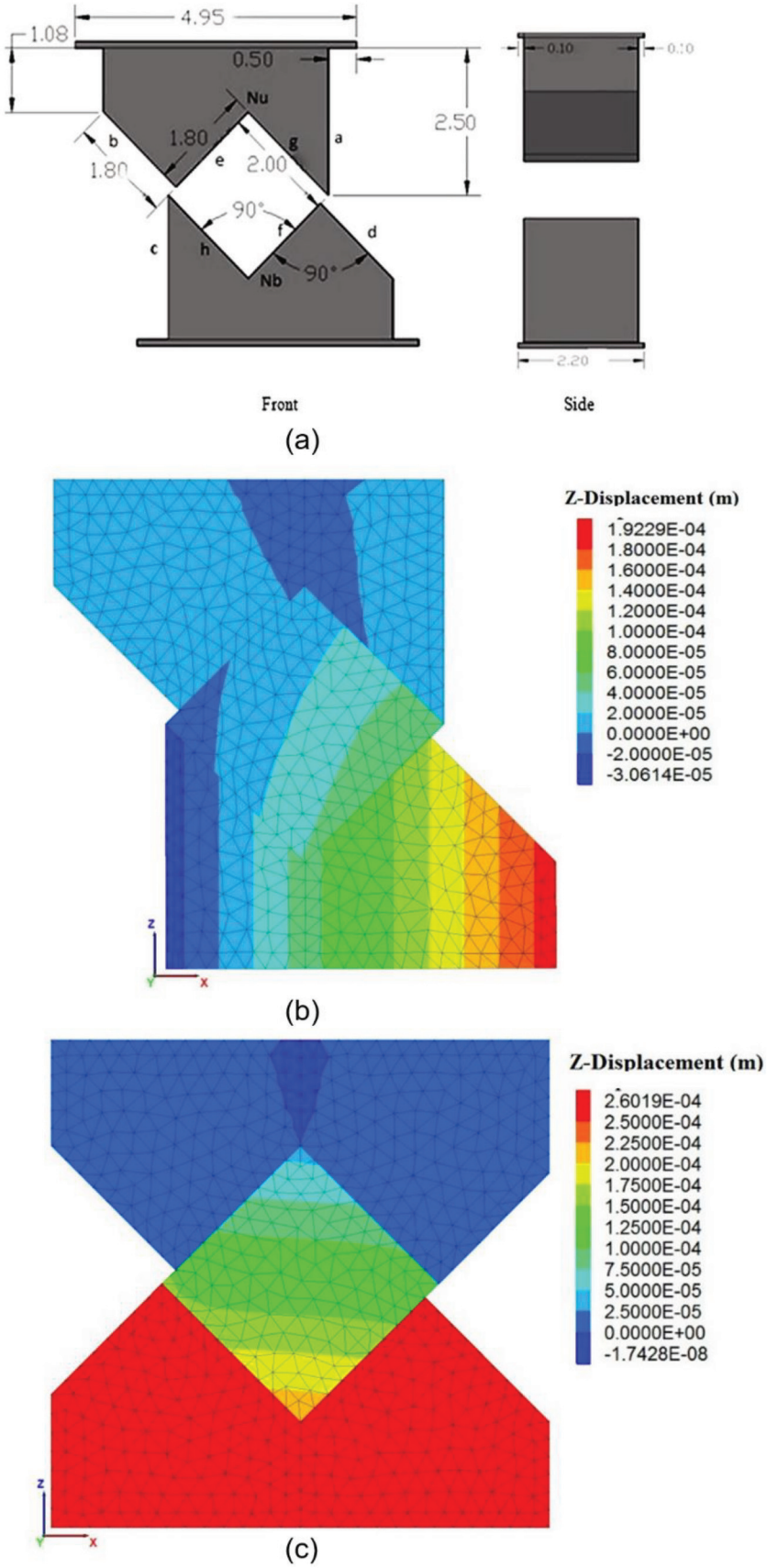

Can. Geotech. J. Downloaded from cdnsciencepub.com by Indian Institute of Science Bengaluru (IISc) on 01/03/22
For personal use only.

Fig. 2. (*a*) CAD drawing of modified biaxial device showing exact dimensions of platens; (*b*) test setup with biaxial platens ($\sigma_1 = \sigma_2$). (All dimensions in millimetres.) [Color online.]

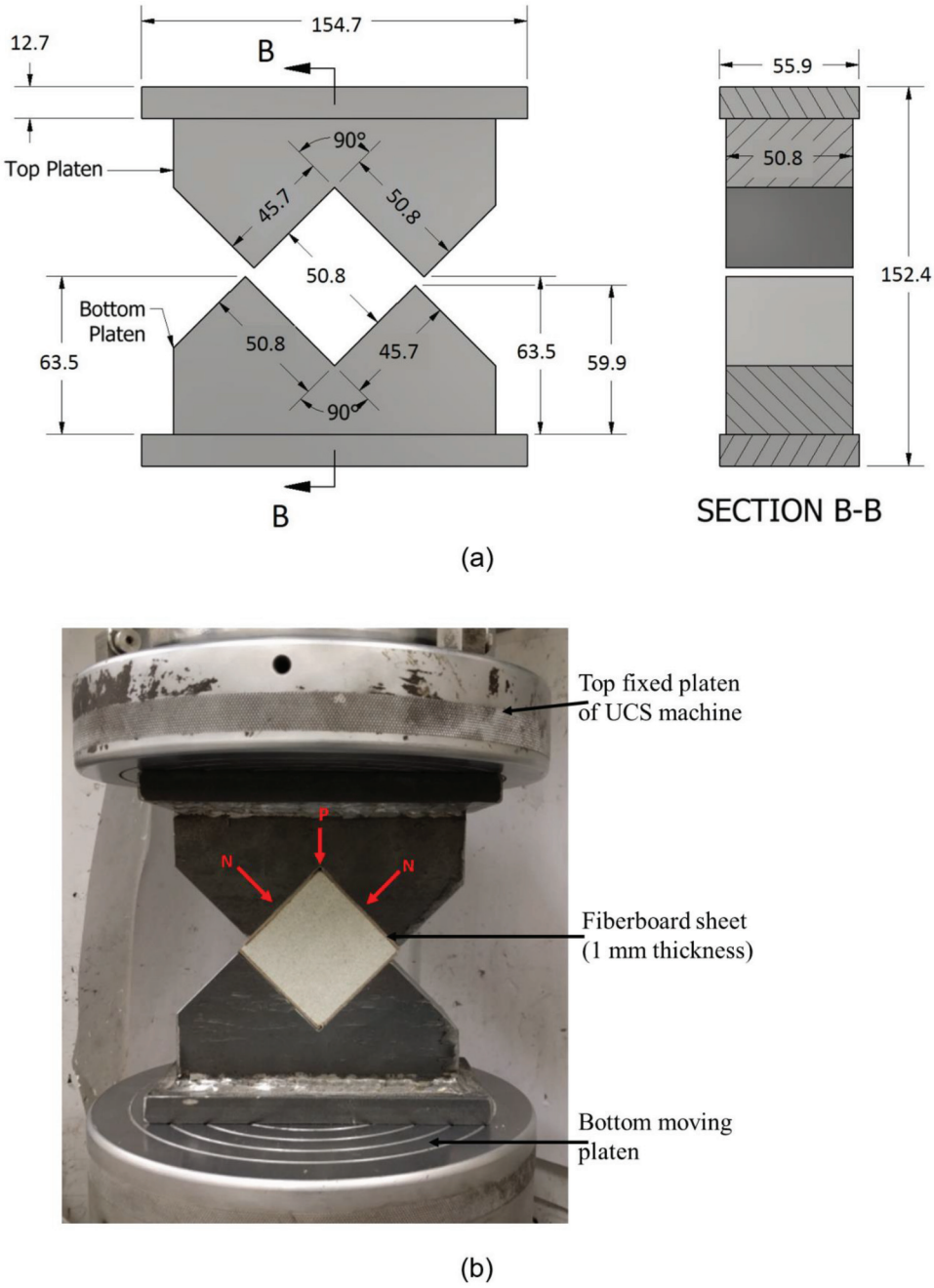

loading on the specimen's end surfaces by removing the effect of circular grooves in the platens of the uniaxial loading device.

3. Testing program

3.1. Specimen preparation

This study analyzed large blocks of Berea sandstone (600 mm × 400 mm × 154 mm) from Cleveland Quarries (Fig. 4*a*). The lithological description is based on X-ray diffraction analysis and information from Cleveland Quarries. The Berea sandstone used in this study is also known as "Liver Rocks". It is homogenous rock with no visible lamination. Mineralogy based on X-ray diffraction analysis shows that this rock mainly includes 90% quartz, 3% dolomite, 7% zeolite, 1% ankerite, and small traces of feldspar and illite (Fig. 4*b*). Ambient porosity is around 18%–20%.

We prepared four groups of specimens from large Berea sandstone blocks, using a machine-operated rock saw to cut the specimens with a circular cutting blade. A mechanized grinding system ground and leveled all the surfaces of the specimen up to a tolerance of +0.20 mm and smoothness with tolerance of Δ/d 0.0043 mm in accordance with standard D4543 (ASTM 1998). The angle between the adjacent face was kept at 90° with a tolerance of 0.250°. We oven-dried the specimens and weighed them repeatedly until no weight loss occurred. The average dry density of Berea sandstone was 2450 kg/m^3. The four groups of specimens tested were:

Can. Geotech. J. Downloaded from cdnsciencepub.com by Indian Institute of Science Bengaluru (IISc) on 01/03/22
For personal use only.

Fig. 3. (*a*) Schematic view of experimental set-up of biaxial test with confining device (σ_2 = constant); (*b*) schematic view of experimental set-up of true-triaxial test (biaxial frame with confining device) replicating $\sigma_1 = \sigma_2 > \sigma_3$ and σ_3 = constant. [Color online.]

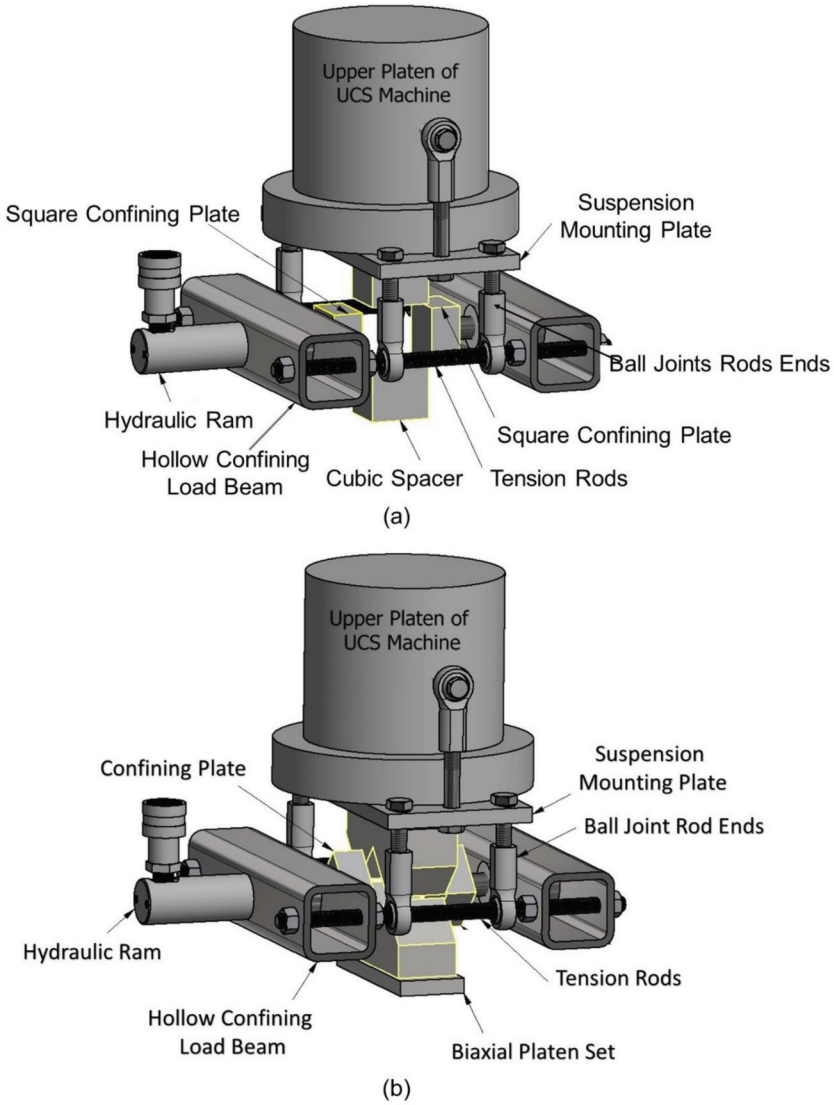

- Group A-Ux-O: cylindrical specimens, 50.8 mm in diameter and 101.6 mm in length, with a height/diameter ratio (*H*/*D*) of 2.
- Group B-Ux-P: prismatic specimens, 50.8 mm × 50.8 mm × 101.6 mm, with a height/width (*H*/*W*) ratio of 2.
- Group C-Ux-Q: cubical specimens, 50.8 mm × 50.8 mm × 50.8 mm, with a height/width (*H*/*W*) ratio of 1.0.
- Group D-Ux-R: prismatic specimens, 50.8 mm × 50.8 mm × 25.4 mm, with a height/width (*H*/*W*) ratio of 0.5.

We used group A to determine the UCS of cylindrical specimens of Berea sandstone. All specimens excluding group A had a square cross section (50.8 mm × 50.8 mm). We used groups labeled "B-Ux-P", "C-Ux-Q", and "D-Ux-R" to study the size effect in uniaxial compressive tests. Additionally, group C also featured in biaxial and true-triaxial tests to validate the platen design and understand the transition in peak strength and failure mode from a uniaxial to a triaxial stress state. Figure 5 shows the geometric shapes of the four groups of specimens.

3.2. Test parameters

As discussed in the previous sections, this study conducted uniaxial tests on four different specimen groups with five specimens for each group (Table 1). We studied the specimens from groups labeled "B-Ux-P", "C-Ux-Q", and "D-Ux-R" for the influence of specimen size; we also compared the peak strength (UCS, also shown as σ_c) with the strength of standard cylindrical specimens from the group labeled "A-Ux-O".

Biaxial tests were conducted on 50.8 mm (2 in.) cubical specimens groups labeled "C-Bx-1-B" and "C-Bx-2-A" for two different loading paths (Figs. 6*a* and 6*b*). In the current study, a rock specimen labeling system was created to represent the experimental stress conditions. For instance, in the specimen group labeled "C-Bx-1-B", "C" represents the cubical specimen, "Bx" represents biaxial compression test, "1" represents the loading path used in the experiment (Fig. 6*a*). The loading path 1 ran using the biaxial frame (Fig. 2*b*), which represented high intermediate stress ($\sigma_1 = \sigma_2$) where both principal stresses increased until failure (Table 2). In loading path 2, the square plates of the confining device applied the constant intermediate stress (σ_2 = constant), and the uniaxial frame increased the maximum principal stress σ_1 until failure (Fig. 3*a*). Additionally, tests under loading path 2 used three intermediate stress levels (σ_2 = 6.9, 13.8, and 27.6 MPa stress).

True-triaxial tests were conducted on 50.8 mm cubical specimens from groups labeled "C-Tx-3-E" and "C-Tx-3-F" using the

Can. Geotech. J. Downloaded from cdnsciencepub.com by Indian Institute of Science Bengaluru (IISc) on 01/03/22
For personal use only.

Fig. 4. (*a*) Berea sandstone from Cleveland Quarries; (*b*) X-ray diffraction peaks for Berea sandstone specimen. [Color online.]

(a)

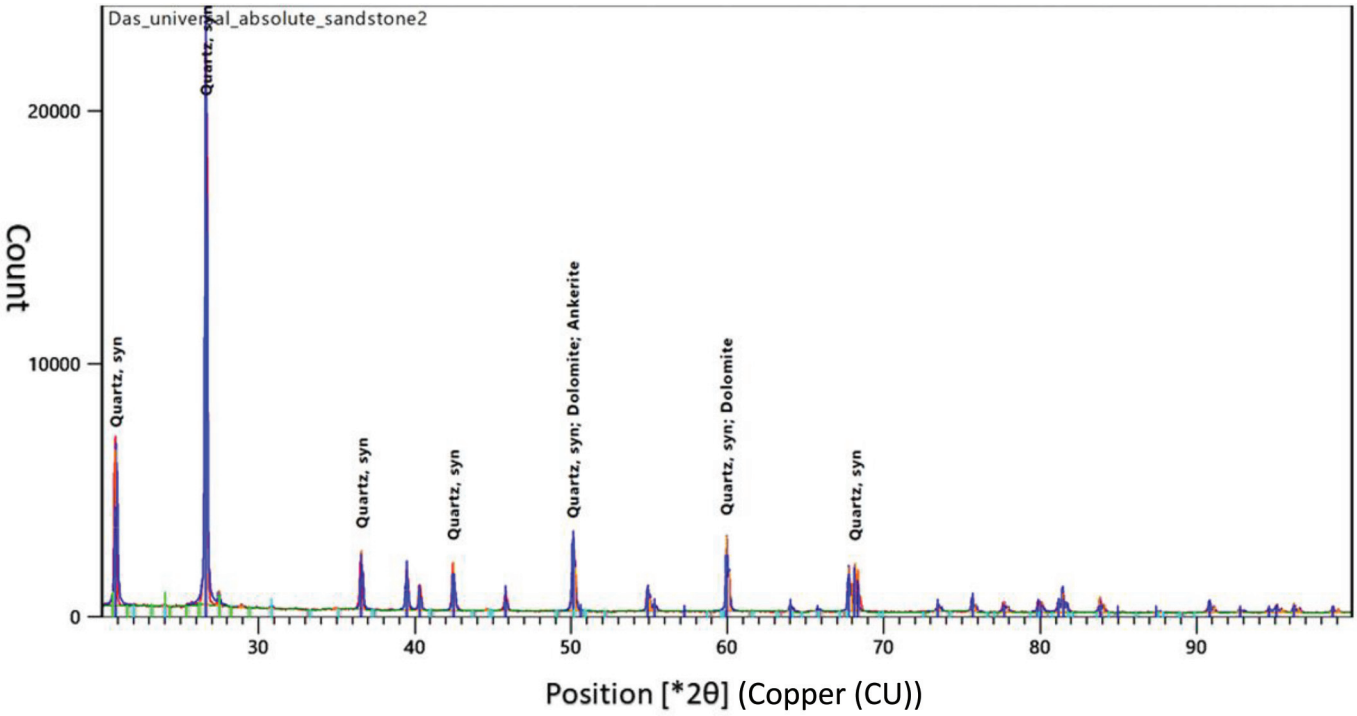

(b)

Can. Geotech. J. Downloaded from cdnsciencepub.com by Indian Institute of Science Bengaluru (IISc) on 01/03/22
For personal use only.

Can. Geotech. J. Downloaded from cdnsciencepub.com by Indian Institute of Science Bengaluru (IISc) on 01/03/22
For personal use only.

Fig. 5. Geometric shapes of four groups of Berea sandstone specimens (*H*, *W* represent height, width of prism specimen, respectively).

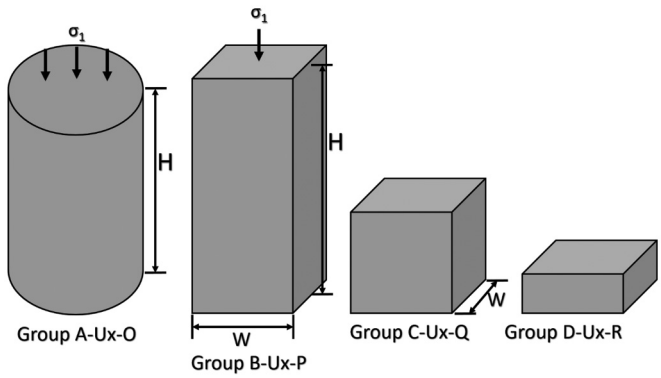

Table 1. List of test parameters used in uniaxial tests.

Group	Specimen shape	Specimen slenderness ratio, *H*/*W*	Number of tests
A-Ux-O	Cylindrical	2	5
B-Ux-P	Cuboidal	2	5
C-Ux-Q	Cubical	1	5
D-Ux-R	Cuboidal	0.5	5

biaxial frame in conjunction with the confining device (Fig. 3*b*). This test follows loading path 3 (Fig. 6*c*), i.e., σ_3 = constant (by confining device) and $\sigma_1 = \sigma_2$ (by biaxial frame) increased until specimen failure. The stress state replicated in this test also corresponds to axisymmetric extension (Ma et al. 2017). These tests ran under three levels of minor principal stress (σ_3 = 0, 6.2, and 20.7 MPa). This study cannot perform higher confinement tests due to the limited load capacity of the confining device. This study tested five specimens for each loading condition and specimen size. Table 2 provides the list of applicable test parameters for biaxial and true-triaxial tests.

This study used displacement control mode to apply load on the rock specimen with a rate of 0.00254 mm/s. The mode loaded the specimen until it exceeded the limit of axial displacement of the platens to avoid any contact between them.

3.3. Post-test analysis

We conducted a post-test analysis to identify the failure modes through photographic images and peak strength. From each test, we recorded the ultimate load from the uniaxial load cell and hydraulic jack (in case of tests with the confining device). We also determined the peak strength based on test conditions. Then, we calculated the corresponding principal stresses σ_1, σ_2, and σ_3 for each test.

For tests with the biaxial device (Figs. 2*b* and 3*a*), we calculated peak stress ($\sigma_1 = \sigma_2$) using approximate stress, acting on the faces of the specimen in contact with the biaxial platen. As shown in Fig. 2*b*, if *P* is the force applied by the platens of the uniaxial loading device, *N* is a component of the force that is acting normal to the face of the specimen, as given by:

$$N = P\cos 45^\circ \tag{1}$$

A_{avg} is the approximate area of the face of the cubical specimen in contact with the biaxial platen, calculated by:

Fig. 6. Biaxial test: (*a*) loading path 1; (*b*) loading path 2 ($n_1\sigma_c$ represents magnitude of constant intermediate stress in terms of average UCS of cubical sandstone); (*c*) loading path 3 (Ma and Haimson 2016) used in true-triaxial testing ($n_2\sigma_c$ represent magnitude of constant minor principal stress in terms of average UCS). [Color online.]

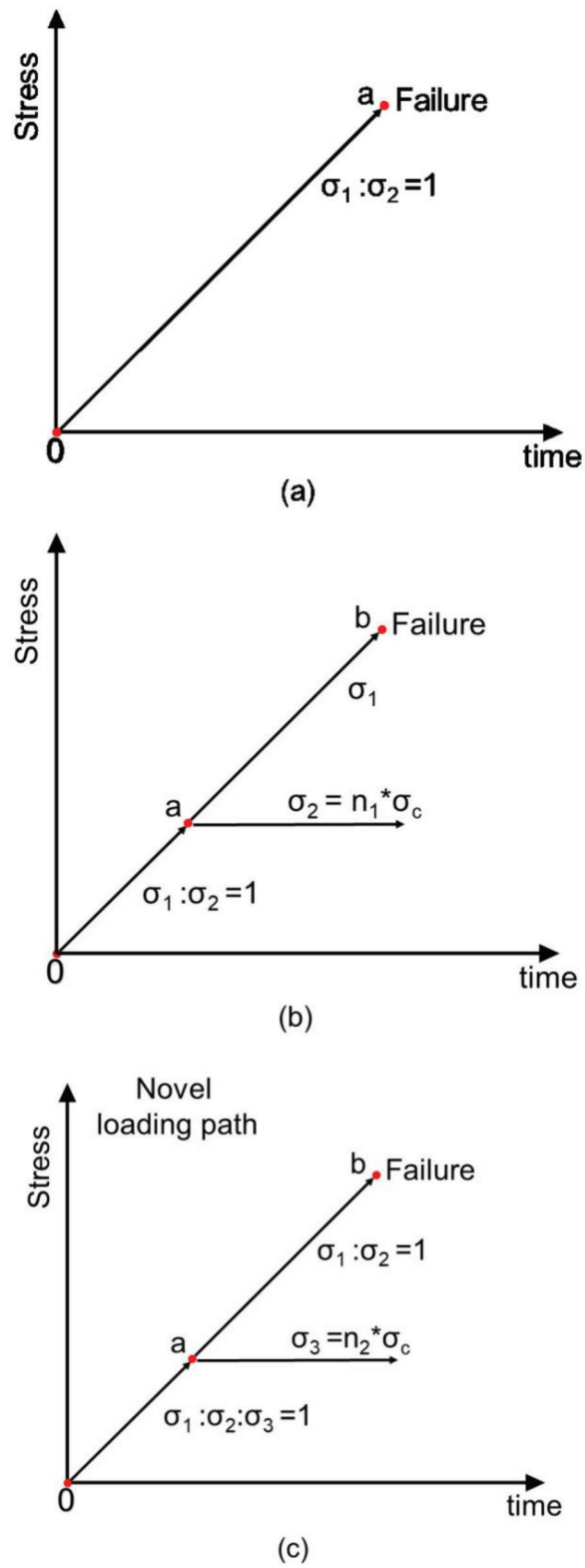

Fig. 7. (*a*) UCS of square-shaped cross section specimens with different slenderness ratios obtained from uniaxial compression test; (*b*) illustration of end effect in specimens with different slenderness ratios in rock uniaxial compression tests (redrawn based on Xu and Cai 2017). τ, frictional stress. [Color online.]

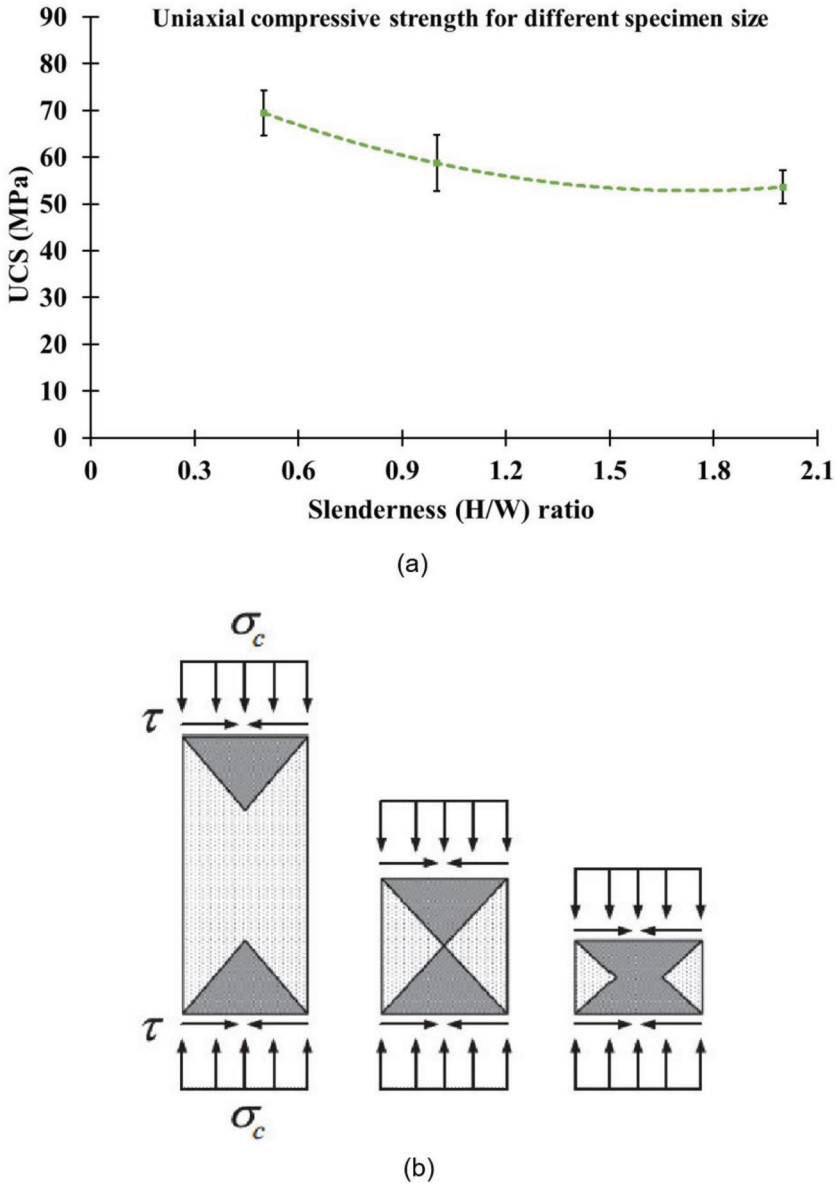

(2) $A_{avg} = (A_1 + A_2)/2$

where A_1 and A_2 are specimen area in contact with adjacent arms of the biaxial platen. The peak stress is given by:

(3) $\sigma_1 = N/A_{avg}$

3.4. Test limitation

Although the design of the biaxial frame and confinement apparatus are simple and cost-effective, there are some limitations in using them, which are as follows:

1. The design limits the specimens that can be tested in the biaxial and true-triaxial apparatus to 50.8 mm cubes.
2. The design did not instrument specimens to obtain strain measurements.
3. The design ignores friction between the biaxial frame and platens of the compression test rig.
4. The design could not completely eliminate friction at rock–platen interface.

Table 2. List of test parameters used in biaxial and true-triaxial test (five tests performed in each case; all specimens had a cubical shape).

Loading path	σ_1/σ_2 stress ratio	σ_3/σ_c stress ratio
1	$\sigma_1 = \sigma_2$	$\sigma_3 = 0$
2	$\sigma_2 = 0.12\sigma_c$ (constant)	$\sigma_3 = 0$
	$\sigma_2 = 0.233\sigma_c$ (constant)	$\sigma_3 = 0$
	$\sigma_2 = 0.46\sigma_c$ (constant)	$\sigma_3 = 0$
3	$\sigma_1 = \sigma_2$	$\sigma_3 = 0$
		$\sigma_3 = 0.11\sigma_c$ (constant)
		$\sigma_3 = 0.35\sigma_c$ (constant)

Can. Geotech. J. Downloaded from cdnsciencepub.com by Indian Institute of Science Bengaluru (IISc) on 01/03/22
For personal use only.

Can. Geotech. J. Downloaded from cdnsciencepub.com by Indian Institute of Science Bengaluru (IISc) on 01/03/22
For personal use only.

Table 3. Results of uniaxial compressive tests.

Group	Specimen shape	Specimen slenderness ratio, H/W	Average UCS (σ_c) ± standard deviation (MPa)
A-Ux-O	Cylindrical	2	50.5 ± 7.5
B-Ux-P	Cuboidal	2	53.6 ± 3.6
C-Ux-Q	Cubical	1	58.7 ± 6
D-Ux-R	Cuboidal	0.5	69.5 ± 4.8

Fig. 8. Experimental results obtained from biaxial tests for different loading paths. [Color online.]

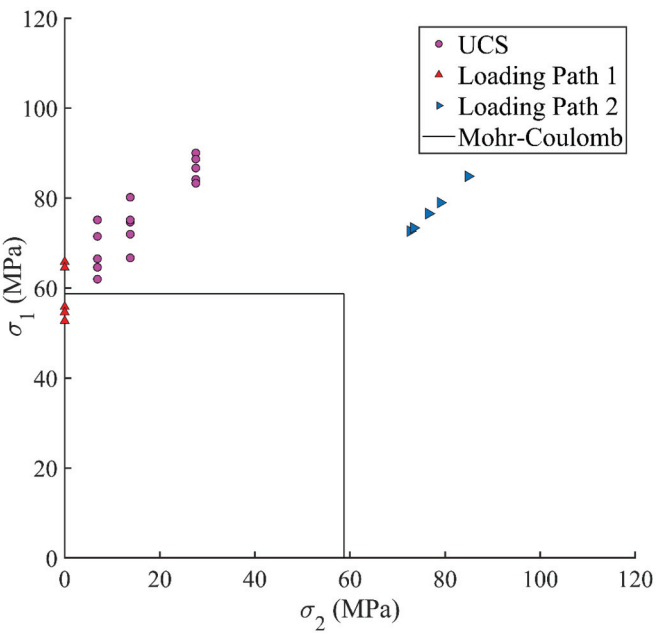

5. The design could not perform true-triaxial test under high confinement due to limited load capacity of the confining device.

4. Test results

4.1. Uniaxial compression strength

This study performed UCS tests on standard cylindrical specimens and prismatic specimens with different slenderness ratios H/W (where H is height of specimen, W is width of specimen), shown in Fig. 5. All the specimens (except group A, which included standard cylinders) had square cross sections (50.8 mm ×50.8 mm). The objective of these tests was to study the change in failure mode of specimens from cylindrical to 50.8 mm cubes. These tests show the influence of specimen size and shape on failure mechanism and its peak strength. Additionally, uniaxial tests on cubical specimens were the baseline for failure mode of poly-axial loading on Berea sandstone. Table 3 provides the test results of uniaxial compressive tests for each group. The average UCS (σ_c) increased by 29.6% (53.6 to 69.5 MPa) as the specimen height decreased from 101.6 mm (H/W = 2) to 25.4 mm (H/W = 0.5), shown in Table 3 and Fig. 7*a*. Researchers have often attributed this trend to the end effect that activates a confined zone near the specimen ends (Xu and Cai 2017). Therefore, as specimen slenderness decreased (or specimen height in this study), the area of the specimen under confinement increased resulting in higher peak strength (Fig. 7*b*).

Table 3 shows that the average UCS value was close to 50.5 MPa in standard cylindrical specimens, which was lower by 6% when compared to prismatic specimens of the same height (around 53.6 MPa). This small increase in the peak strength from circular to square-shaped cross section suggested limited influence of cross-sectional shape on the UCS of sandstone, similar to results by Xu and Cai (2017).

Table 4. Results of biaxial tests and true-triaxial tests.

Specimen index	Loading path	σ_3/σ_c stress ratio	Average stress σ_1 ± standard deviation (MPa)	σ_2 (MPa)	σ_3 (MPa)
C-Bx-2-A	2	0	68 ± 4.8	6.9	0
C-Bx-2-B	2	0	73.7 ± 4.4	13.8	0
C-Bx-2-C	2	0	87.2 ± 3.3	27.6	0
C-Bx-1-D	1	0	77.3 ± 4.4	77.3	0
C-Tx-3-E	3	0.11	98.9 ± 5.2	98.9	6.2
C-Tx-3-F	3	0.35	136.7 ± 10.2	136.7	20.7

4.2. Biaxial compressive test

Table 4 presents the average peak strength data and corresponding principal stresses of each test condition. Figure 8 shows the results from biaxial tests plotted as peak strength, σ_1 (major principal stress), against corresponding intermediate principal stress, σ_2. For loading path 2, the peak strength σ_1 increased with the increase in the intermediate principal stress, σ_2. The average peak strength, σ_{1avg} increased from 67.9 to 73.7 MPa as σ_2 increased from 6.9 to 13.8 MPa (Table 4). The percentage increase in the peak strength was around 15.72% and 25.56% from its UCS value (58.7 MPa) for constant σ_2 = 6.9 and 13.8 MPa, respectively. The average peak strength further increased to 87.2 MPa (Table 4) as σ_2 increased to 0.46σ_c (27.6 MPa). However, for loading path 1, which represents high intermediate stress ($\sigma_1 = \sigma_2$), the peak strength decreased to 77.3 MPa. Although the peak strength for load path 1 was lower compared to tests when σ_2 = 0.45σ_c under loading path 2 (Fig. 8), it is still 1.31 times the UCS value. We concluded that the biaxial strength of sandstone is higher than its uniaxial equivalent at any level of intermediate principal stress with maximum strength around σ_2 = 0.45σ_c. Yun et al. (2008, 2010) showed similar observations for granite and coalmine sandstone rocks: that the peak strength, σ_1, was highest for $\sigma_2 \sim 0.5\sigma_c$ and decreased under high intermediate principal stress, i.e., $\sigma_1 = \sigma_2$.

4.3. True-triaxial test

True-triaxial tests on 50.8 mm cubical specimens used the biaxial frame in conjunction with the confining device (Fig. 3*b*), representing loading path 3, $\sigma_1 = \sigma_2$ and σ_3 = constant (Fig. 6*c*) and corresponds to triaxial extension (Ma et al. 2017) instead of compression test due to high intermediate stress, σ_2. Table 4 presents peak strength data along with the corresponding principal stresses of each test.

Figure 9*a* plots the failure data points from true-triaxial tests as peak strength σ_1 against corresponding minor principal stress, σ_3. As confinement σ_3 increases, peak strength σ_1 also increases. However, this plot does not clearly reflect the effect of intermediate principal stress, as it does not take into account the influence of load path (Ma and Haimson 2016). Therefore, two principal stress invariants represent the failure results (Fig. 9*b*): the octahedral shear stress at failure, $\tau_{oct,f}$, and the octahedral normal stress at failure, $\sigma_{oct,f}$.

5. Poly-axial strength criteria

5.1. Biaxial strength criteria

The two most prevalent failure criteria, Mohr–Coulomb and Hoek–Brown, exclude the influence of intermediate principal stress, σ_2, as they only consider σ_1 and σ_3. In theory, the intermediate principal stress does not contribute to the strength of the rock specimen; consequently, the uniaxial and biaxial compressive

Can. Geotech. J. Downloaded from cdnsciencepub.com by Indian Institute of Science Bengaluru (IISc) on 01/03/22
For personal use only.

Fig. 9. (*a*) Variation of σ_1 (peak strength) with σ_3 in Berea sandstone for axisymmetric loading conditions ($\sigma_1 = \sigma_2$ and σ_3 = constant); (*b*) variation of octahedral shear at failure ($\tau_{oct,f}$) with octahedral normal stress ($\sigma_{oct,f}$) in Berea sandstones for axisymmetric loading conditions ($\sigma_1 = \sigma_2$ and σ_3 = constant). [Color online.]

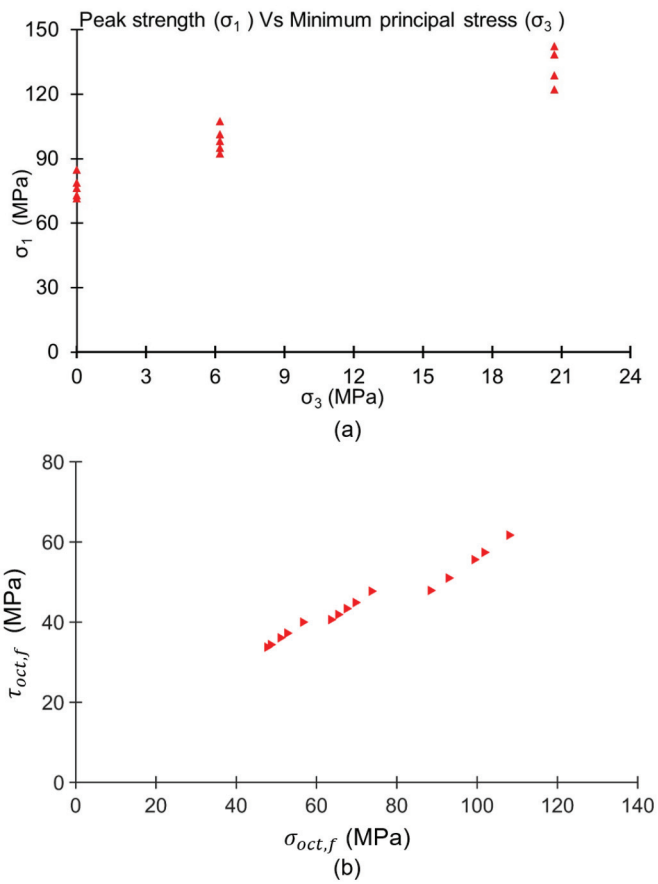

strengths should be the same. However, this was not the case for the Berea sandstone as seen in Figs. 8 and 10. Therefore, these criteria are not suitable for biaxial or plane stress conditions.

The Drucker–Prager failure criterion (Drucker and Prager 1952) is well-known for its application to brittle materials such as concrete and rock. This criterion accounts for the influence of all principal stresses and is expressed by using the invariants of the stress tensor:

$$(4) \qquad \boldsymbol{F} = \alpha I_1 + J_2^2 - k = 0$$

where α and k are material constants and can be expressed in terms of friction angle, ϕ, and cohesion, c, of the material, I_1 and J_2 stress invariants.

$$(5) \qquad I_1 = \sigma_1 + \sigma_2 + \sigma_3$$

$$(6) \qquad J_2 = [(\sigma_1 - \sigma_2)^2 + (\sigma_2 - \sigma_3)^2 + (\sigma_3 - \sigma_1)^2]/6$$

$$(7) \qquad \alpha = \frac{2\sin\phi}{\sqrt{3}(3 - \sin\phi)}$$

$$(8) \qquad k = \frac{6c\cos\phi}{\sqrt{3}(3 - \sin\phi)}$$

In the case of biaxial stress state, $\sigma_3 = 0$ eq. 4 can be rewritten as:

$$(9) \qquad \alpha(\sigma_1 + \sigma_2) + \sqrt{\frac{(\sigma_1^2 - \sigma_1\sigma_2 + \sigma_2^2)}{3}} = k$$

Based on the average value of σ_c for investigated cubical rock specimens, the cohesion c of the rock for corresponding internal frictional angles, ϕ, can be calculated.

$$(10) \qquad c = \frac{\sigma_c}{2}\left(\frac{1 - \sin\phi}{\cos\phi}\right)$$

In turn, we plotted a series of Drucker–Prager failure envelopes in σ_1–σ_2 coordinates and then compared them with experimental failure points to find fitted degree between the Drucker–Prager criterion and experimental results.

Based on the rock failure data, this study used the previous approach to compare Mohr–Coulomb, Hoek–Brown, and Drucker–Prager failure envelopes within $\sigma_1 - \sigma_2$ coordinates, as shown in Fig. 10*a*. For Drucker–Prager criterion, this approach generated a series of envelopes for different friction angles, ϕ (ϕ = 0°–25°), for a given σ_c (from test results). The specific friction angle chosen had "goodness of fit" to the experimental results. Though data points at constant confinement (σ_2 = 0, 6.9, 13.8, and 27.6 MPa) are scattered, ϕ = 0°–25° provides the best "fit" with failure points at confining stress less than 28 MPa ($\sigma_2 < \sigma_c/2$). However, for the $\sigma_1 = \sigma_2$ condition, the friction angle of 15° was the best "fit" with corresponding failure points (Fig. 10*a*). The analysis demonstrated that while Drucker–Prager criterion accounts for the influence of intermediate stress, it provides poor correlation with biaxial test results of Berea sandstone. This conclusion was in good agreement with the study by Al-Ajmi and Zimmerman (2005), which showed that Drucker–Prager criterion is usually inappropriate for most rocks. Furthermore, both Mohr–Coulomb and Hoek–Brown criteria substantially underestimated the biaxial strength of cubical sandstone specimen (Fig. 10*a*) under the condition of $\sigma_3 = 0$.

As no standard criteria fit the failure data points of Berea sandstone, we performed a regression analysis to determine the best-fit polynomial curve (Fig. 10*b*). The analysis found a quadratic polynomial with R^2 of 0.7507 to be the best fit for the biaxial tests data points of cubical sandstone specimens:

$$(11) \qquad \sigma_1 = -0.0133\sigma_2^2 + 1.2797\sigma_2 + 58.969$$

Equation 11 shows the mean value of coefficients of regression polynomial. The 95% confidence interval of the coefficients of σ_2^2, σ_2, and constant was obtained as (–0.0175 to –0.0085), (0.878 to 1.632), (55.17 to 63.95), respectively. Figure 10*b* showed failure stress data plotted against both Mohr–Coulomb and Hoek–Brown criteria, as well as the best-fitted polynomial curve for the experimental results of sandstone specimen. From these data, we inferred that the specimen exhibits a maximum strength of approximately 89.8 ± 23.2 MPa at intermediate principal stress (σ_2) of 48 MPa, which is nearly 1.5 times the average uniaxial strength of 50.8 mm cubical specimens. A similar trend in change in the failure strength (σ_1) with an increase in intermediate principal stress (σ_2) was found by other studies (Yun et al. 2008, 2010; Du et al. 2020) on various rock types such as granite, marble, and sandstone, coalmine sandstone, etc. The specimen under constant intermediate principal stress (σ_2) of 48 MPa cannot be tested due to the limited capacity of the biaxial device used in the current study. It can only apply constant intermediate principal stress (σ_2) up to 28 MPa.

5.2. True-triaxial strength envelope in terms of principal stress invariants $\tau_{oct,f}$ and $\sigma_{oct,f}$

As mentioned in previous sections, there is a significant influence of intermediate principal stress on the failure strength of sandstone under biaxial and triaxial stress state. Various researchers have comprehensively investigated the influence of intermediate

Fig. 10. (*a*) Drucker–Prager criteria with experimental data points (EDP) at failure; (*b*) polynomial regression curve with EDP at failure. [Color online.]

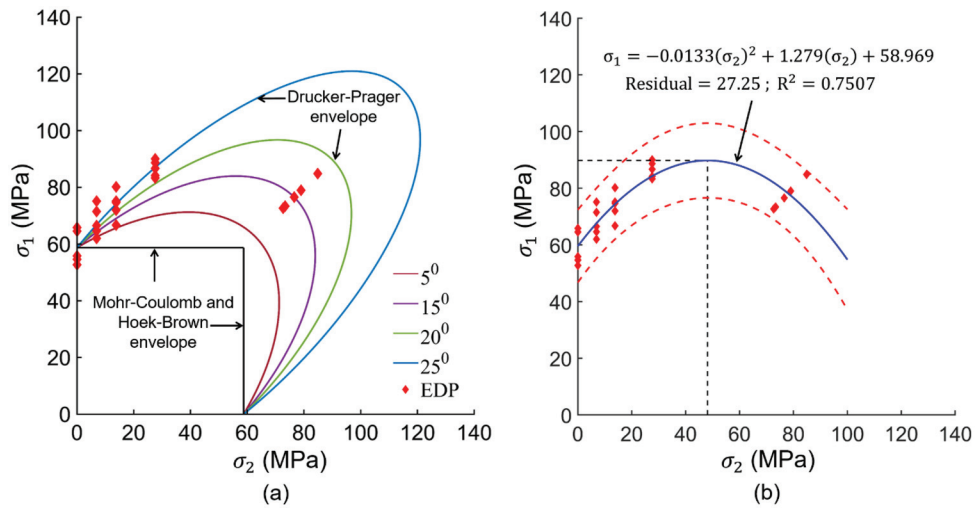

principal stress on rock strengths (Handin et al. 1967; Colmenares and Zoback 2002; Al-Ajmi and Zimmerman 2005). Several failure criteria have included the intermediate principal stress to describe rock strength under true-triaxial stress states, e.g., modified Wiebols and Cook (1968) criterion and Mogi (1971) criterion.

For porous sandstone rocks, most of preceding failure criteria do not fit well with experimental results due to the formation of a compaction band under high in situ stresses (Ma 2014). There are some failure criteria such as Nadai (1950) criterion, Lade and Duncan (1975) criterion, Matsuoka and Nakai (1974) criterion, and modified Matsuoka–Nakai–Lade–Duncan criterion (Rudnicki 2013) that are applicable to sandstones. However, most of these criteria require extensive experimental data to get "best-fit" criterion for a particular sandstone. The current study only ran true-triaxial tests for three confinement levels (i.e., σ_3 = 0, 6.2, and 20.7 MPa) due to the limitation of the confining device. Hence, this study tested Nadai (1950) criterion to see whether it can provide the "best-fit" for the experimental data.

Nadai (1950) proposed a three-dimensional (3D) failure criterion for brittle materials. He suggested that the failure envelope could be represented by a single relationship in terms of the two principal stress invariants. The failure will occur when distortional strain energy reaches the critical value and is the function of octahedral normal stress given by:

$$\tau_{\mathrm{oct,f}} = f(\sigma_{\mathrm{oct,f}}) \tag{12}$$

where $\tau_{\mathrm{oct,f}}$ and $\sigma_{\mathrm{oct,f}}$ are octahedral shear stress at failure and the octahedral normal stress at failure, respectively, and are defined in terms of principal stresses as follows:

$$\tau_{\mathrm{oct,f}} = \frac{1}{3}\sqrt{(\sigma_1-\sigma_2)^2+(\sigma_2-\sigma_3)^2+(\sigma_3-\sigma_1)^2} \tag{13}$$

$$\sigma_{\mathrm{oct,f}} = (\sigma_1+\sigma_2+\sigma_3)/3 \tag{14}$$

The function "*f*" is determined from the best fitting curves for a particular rock and generally can either be a second order polynomial or a power law. For porous sandstone rocks, the best-fit function is preferred to be a quadratic equation (Olsson 1999; Ma 2014). Figure 11 shows failure data points of Berea sandstone for loading path $\sigma_1 = \sigma_2$ and σ_3 = constant, fitted by the quadratic equation with R^2 of 0.964 as shown:

Fig. 11. Triaxial strength envelop based on Nadai criterion (Nadai 1950) fitted with EDP at failure for axisymmetric loading conditions ($\sigma_1 = \sigma_2$ and σ_3 = constant). [Color online.]

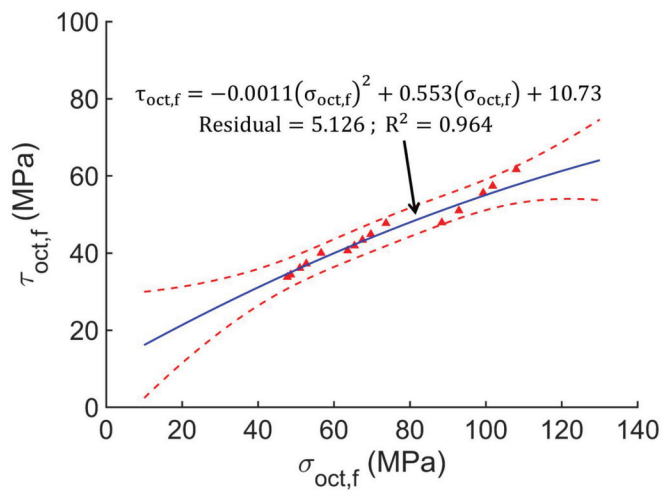

$$\tau_{\mathrm{oct,f}} = -0.0011\sigma_{\mathrm{oct,f}}^2 + 0.553\sigma_{\mathrm{oct,f}} + 10.73 \tag{15}$$

Equation 15 shows the mean value of coefficients of the quadratic polynomial obtained using regression. The 95% confidence interval of the coefficients of $\sigma_{\mathrm{oct,f}}^2$, $\sigma_{\mathrm{oct,f}}$, and constant were obtained as (–0.0045 to 0.0023), (0.041 to 1.06), (–7.28 to 28.85), respectively. Although data points are scattered, we observed that the average $\tau_{\mathrm{oct,f}}$ increased with increase in $\sigma_{\mathrm{oct,f}}$. Ma and Haimson (2016) showed similar observations for Bentheim and Coconino sandstones. Additionally, for Bentheim sandstone, Ma et al. (2017) found a "cap" value of $\sigma_{\mathrm{oct,f}}$, at which $\tau_{\mathrm{oct,f}}$ would be the maximum value and then gradually decline. Studies generally observe the cap value at a very high level of confinement (Olsson 1999; Ma et al. 2017). For instance, for Bentheim sandstone, "cap" occurs at σ_3 = 285.4 MPa, which is 9.5 times its UCS (Ma et al. 2017). However, the current study did not find this cap for Berea sandstone, as the level of confinement under true-triaxial testing was limited to 20.7 MPa.

Can. Geotech. J. Downloaded from cdnsciencepub.com by Indian Institute of Science Bengaluru (IISc) on 01/03/22
For personal use only.

Fig. 12. (*a*) Dominant shear failure with spalling at outer surface in cuboidal specimen of 101.16 mm height (*H*/*W* = 2); (*b*) cross-shear failure of inner core along with spalling at outer surface in cubical specimen of 50.8 mm height (*H*/*W* = 1); (*c*) hourglass type failure cuboidal specimen of 25.4 mm height specimen (*H*/*W* = 1/2). [Color online.]

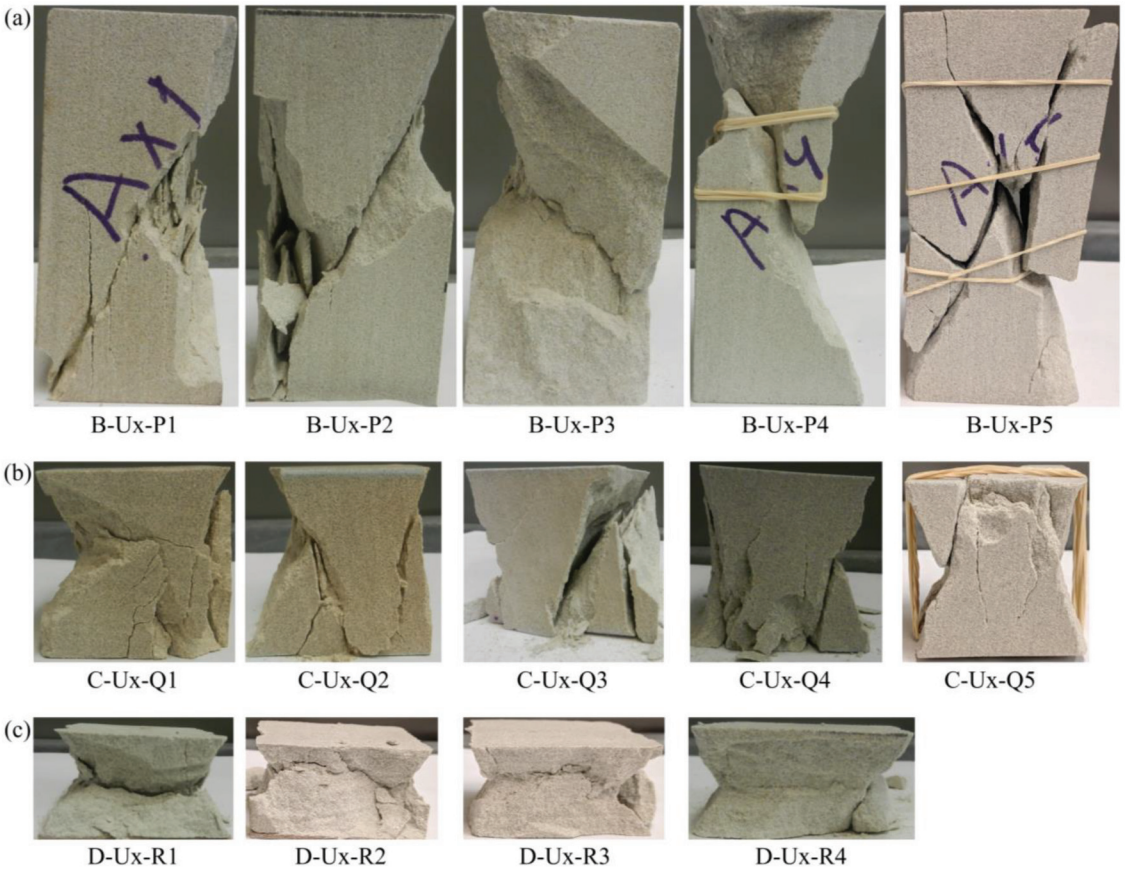

Can. Geotech. J. Downloaded from cdnsciencepub.com by Indian Institute of Science Bengaluru (IISc) on 01/03/22
For personal use only.

6. Failure mechanism

6.1. Influence of specimen size on failure of Berea sandstone

Figure 12 shows the transition of failure mode as the slenderness ratio (*H*/*W*) of sandstone specimen decreased from 2 to 0.5 after uniaxial compression testing. In all specimens under uniaxial load, spalling occurred at free faces, followed by violent failure of the central portion (Fig. 12). A dominant single shear plane (Fig. 12*a*) was observed in the central region of most specimens with *H*/*W* ratio of 2 with the exception of one sample (B-Ux-P5). For specimens with *H*/*W* ratio equal to 1, cross-shear failure occurred in the inner core, resulting in the conical–pyramidal shape in all five specimens (Fig. 12*b*). Additionally, the extent of spalling has increased with a decrease in the specimen's slenderness ratio (*H*/*W*) to 0.5 in which large spalling occurred in a V-shaped region extending from the outer surface to the central portion (Fig. 12*c*). As a result, the hourglass-type failure occurred in all four specimens with *H*/*W* ratio of 0.5 (Fig. 12*c*). Due to the violent failure of Berea sandstone, only four specimens with *H*/*W* ratio of 0.5 were recovered at the end of the test.

The change in failure mode with specimen size is attributed to end effect, as shown in Fig. 7*b*. Feng et al. (2017) investigated the failure mechanism for different specimen sizes using extended finite element method (XFEM) based numerical code. Their study analyzed the crack evolution at different stages of loading, which represents the transition from intact to fractured rock, to understand the friction effect caused by end constraint. Feng et al. (2017) found that in specimens with *H*/*W* ratio equal to 2, end constraint created only a small region of confinement near the specimen ends (similar to Fig. 7*b*, thereby allowing the meso-cracks to initiate around the center of the specimen. These cracks propagate towards the outer surface in a diagonal direction, which is a region of low confinement. Similarly, a localized shear band (due to gradual coalesce of cracks) formed, resulting in the development of a shear failure plane across specimen height, similar to Fig. 12*a*. In the case of *H*/*W* = 1, the confined region is much larger, but has no overlapping; this provides an unconfined zone around the center of the specimen (Fig. 7*b*) and allows some meso-cracks to initiate around the specimen center. However, the majority of cracks will form in the low confined region near the outer surface, resulting in significant spalling in that region. These cracks at the outer region may propagate towards the center of the specimen, resulting in the formation of a shear plane similar to Fig. 12*b*. In the case of *H*/*W* = 0.5, the confined regions from the specimen end up overlapping (Fig. 7*b*), causing meso-cracks to form at the outer surface. These cracks propagate and coalesce towards the center, forming opposite vertex cone areas and resulting in hourglass failure (Feng et al. 2017), shown in Fig. 12*c*.

6.2. Influence of loading path on failure of Berea sandstone under biaxial stress state

We performed an analysis on the transition of failure mode from uniaxial to biaxial stress conditions to understand the failure mechanism of sandstone specimens in the biaxial stress state. In the uniaxial stress state, all five specimens exhibited spalling on all free faces of the specimen, followed by violent failure at the mid-section (Fig. 12*b*). The mid-section of the all the five specimens mostly failed in shear with multiple planes intersecting one another (Fig. 12*b*). These failure planes oriented in the

Fig. 13. Failure mode of sandstone samples in uniaxial test: (*a*) σ_1–σ_2 plane; (*b*) σ_2–σ_3 plane. [Color online.]

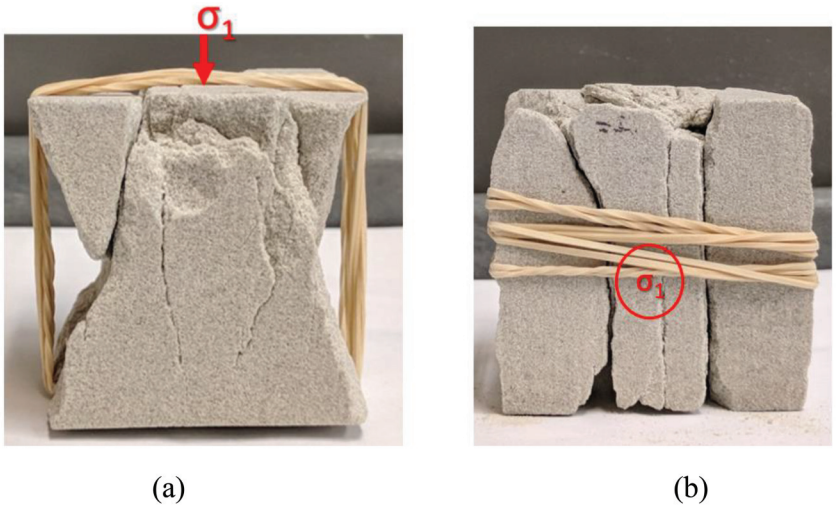

Fig. 14. Failure mode of sandstone samples in biaxial test with loading path 2 at (*a*) σ_2 = 6.9 MPa; (*b*) σ_2 = 13.8 MPa; (*c*) σ_2 = 27.6 MPa. [Color online.]

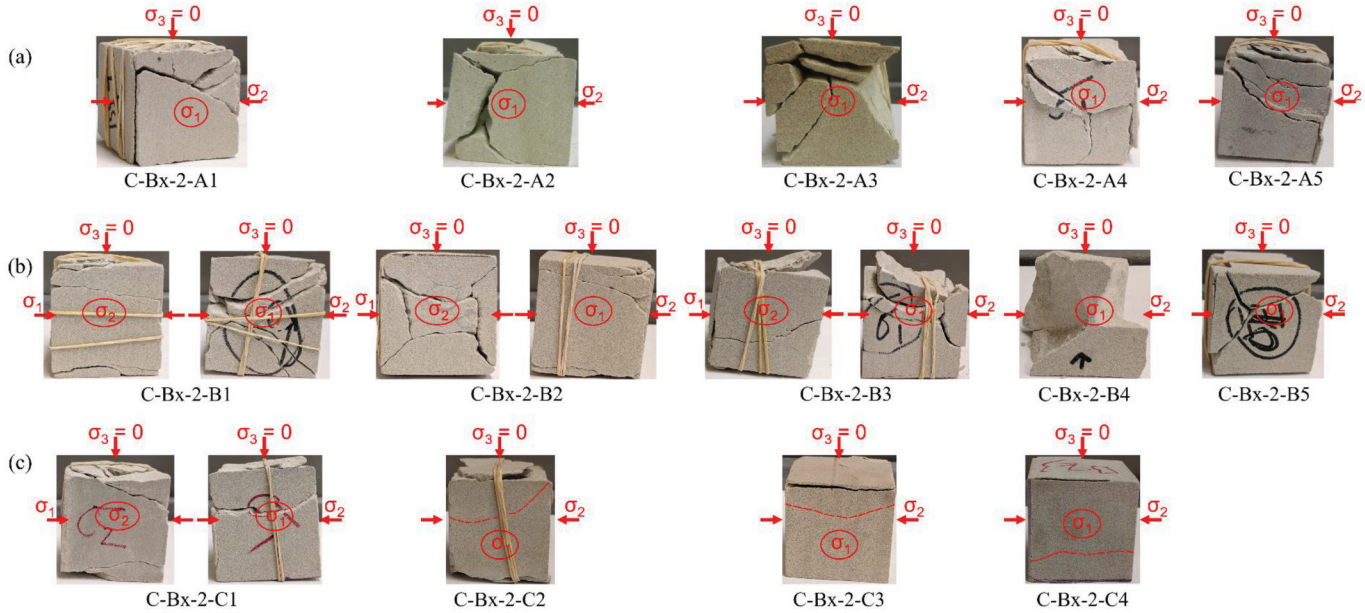

$\sigma_1 - \sigma_2/\sigma_1 - \sigma_3$ plane, leaving a conical or pyramid-like-shaped central portion (Figs. 12*b* and 13).

When testing specimens biaxially, the failure exhibited varying degrees of spalling at the free faces. Figure 14 shows the typical failure mechanism in specimens subjected to the biaxial test under load path 2 (i.e., σ_2 = constant). At σ_2 = 6.9 MPa, five specimens exhibited some degree of spalling at the free faces. It was followed by failure of the central region, which underwent dominant shear failure in three specimens (C-Bx-2-A1, C-Bx-2-A2, and C-Bx-2-A3), while in the remaining two specimens the dominant failure mode is not clearly identifiable (Fig. 14*a*). The dominant failure plane in most of the specimens was oriented in the σ_2–σ_3 plane along with the strike in the σ_1 direction. When the confinement (σ_2) increased to 13.8 MPa (Fig. 14*b*), shear failure was found to be the dominant failure mode in the central region of most of the five specimens except one sample (C-Bx-2-B3). Additionally, the dominant shear failure plane for three specimens (C-Bx-2-B1, C-Bx-2-B2, and C-Bx-2-B3) has a dip, which is a combination of both σ_2–σ_3 and σ_1–σ_3 plane (Fig. 14*b*). While in specimen C-Bx-2-B4, it is not clear that shearing also occurred in the σ_1–σ_3 plane as only one view was captured for this sample (Fig. 14*b*). When intermediate stress further increased to 27.6 MPa (σ_2 = 0.45σ_c), no shearing occurred in the σ_2–σ_3 plane of all four recovered specimens at the end of the test. Additionally, one specimen (C-Bx-2-C1) clearly showed predominant shear failure, which was oriented in the σ_1–σ_3 plane along with strike in the σ_2 direction (Fig. 14*c*). The failure mode in the remaining three specimens (C-Bx-2-C2, C-Bx-2-C3, and C-Bx-2-C4) is unclear as only one view was captured for them (Fig. 14*c*). Yun et al. (2008, 2010) had the similar observation that under high intermediate stress, shearing occurred in the central section of a cubical specimen with its strike in the σ_2 direction. We concluded that from the biaxial tests on sandstone samples under loading path 2, shear failure plane rotated with the increase in intermediate principal stress, σ_2.

For specimens subjected to the biaxial compression test under load path 1 (σ_1 = σ_2), only four specimens out of five tested

Can. Geotech. J. Downloaded from cdnsciencepub.com by Indian Institute of Science Bengaluru (IISc) on 01/03/22
For personal use only.

Can. Geotech. J. Downloaded from cdnsciencepub.com by Indian Institute of Science Bengaluru (IISc) on 01/03/22
For personal use only.

Fig. 15. Failure mode of sandstone samples in (*a*) biaxial test with loading path 1; (*b*) true-triaxial test under σ_3 of 6.2 MPa; (*c*) true-triaxial test under σ_3 of 20.7 MPa. [Color online.]

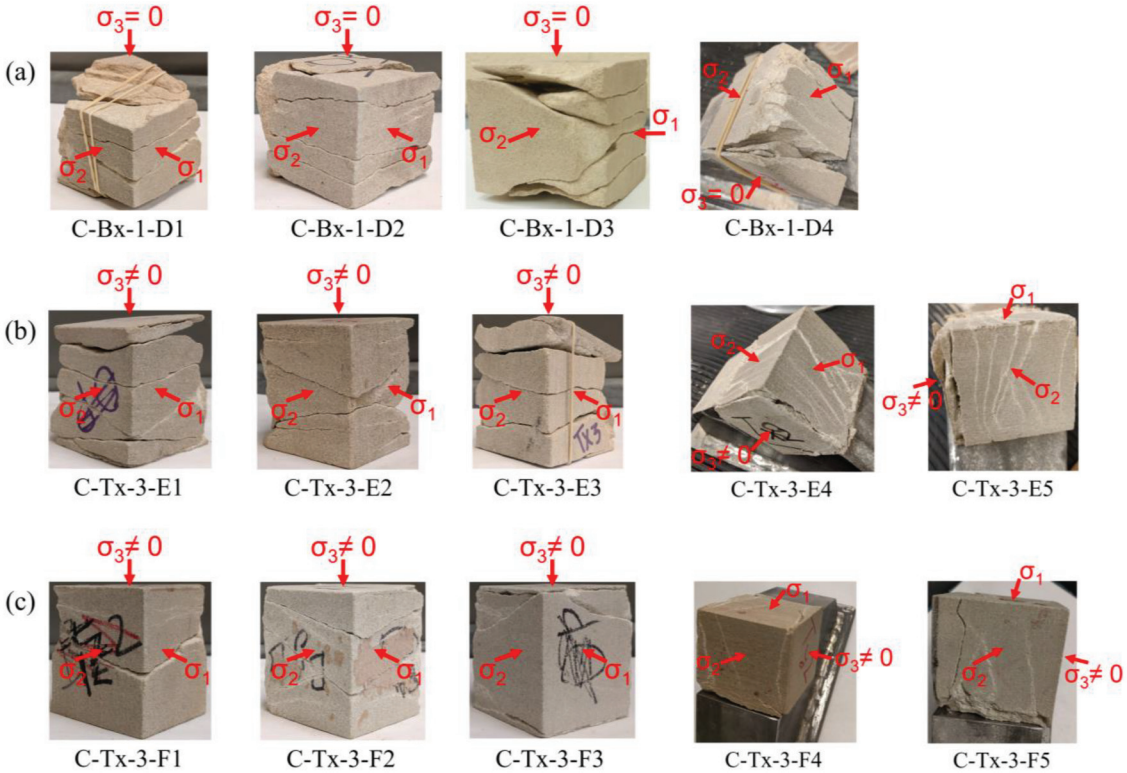

specimens were recovered at the end of the test. (Fig. 15*a*). The failure is characterized by splitting that occupied a large portion of specimen volume in all four specimens (Fig. 15*a*). Furthermore, these splitting planes in all four specimens are nearly perpendicular to the unconfined direction ($\sigma_3 = 0$) with dip and strike direction in the σ_1–σ_2 plane. The remaining central portion in three specimens (C-Bx-1-D1, C-Bx-1-D2, and C-Bx-1-D3) has failed under shear with the strike that is a combination of both σ_1 and σ_2 axis (Fig. 15*a*), while the mode of dominant failure is unclear in the fourth sample (C-Bx-1-D4). Therefore, the dominant shear plane has rotated as compared to the test with load path 2 (σ_2 = 27.6 MPa), where its strike was along the σ_2 axis.

6.3. Influence of confinement on failure mode under true-triaxial tests of cubical sandstone

We analyzed the transition of failure mode from biaxial to triaxial stress conditions to understand the failure mechanism of sandstone specimens under poly-axial stress state. Figure 15 shows typical failure mechanism for novel loading path, i.e., $\sigma_1 = \sigma_2$ and σ_3 = 0–20.7 MPa. For specimens tested biaxially, splitting occupied a large portion of specimen volume as suggested by planes being nearly perpendicular to the unconfined direction (σ_3 = 0) (Fig. 15*a*). The remaining central portion of three specimens (C-Bx-1-D1, C-Bx-1-D2, and C-Bx-1-D3) failed under shear with its strike being a combination of both σ_1 and σ_2 axis.

However, when applying confinement at free surfaces in true-triaxial tests, the extent of the specimen's volume under splitting decreased with an increase in the minor principal stress (σ_3). At σ_3 = 6.2 MPa, splitting still occurred in a significant portion of the volume of all five specimens (Fig. 15*b*). However, these splitting planes are relatively more inclined than the results from the biaxial test (Figs. 15*a* and 15*b*). Additionally, the central portion failed under multiple shear planes in most of the specimens except one sample (C-Tx-3-E3) (Fig. 15*b*). For true-triaxial tests with higher confinement (σ_3 = 20.7 MPa), most of the five specimens predominately failed with one or two shear planes (Fig. 15*c*). Additionally, no or very small splitting was observed in all specimens as compared to the case of σ_3 at 6.2 MPa (Figs. 15*b* and 15*c*). The decrease in the extent of splitting is likely due to the increase in the ductile behavior of sandstone with the increase in confinement. Additionally, the increase in confinement (σ_3) also resulted in the decrease in the area of the specimen under failure from almost the entire specimen under axial splitting in the case of σ_3 = 0 MPa to a single shear plane in its central portion under σ_3 = 20.7 MPa.

7. Conclusion

In this study, we built a new biaxial frame based on the modified design of the biaxial device by Arora and Mishra (2015). The tests ran on 50.8 mm cubical specimens using the biaxial device to replicate the failure of rock under high horizontal loading. In addition to these platens, we used a confining device to conduct tests under limited true-triaxial loading conditions. To validate the biaxial frame and confining device design, we further studied the influence of poly-axial stress state on failure response of Berea sandstone. Additionally, the confining device also helped to determine the influence of loading path on its peak strength and failure mode under biaxial stress state. Based on the laboratory investigation, we have made the following conclusions:

- The average uniaxial compressive strength (UCS, also shown as σ_c) showed an increase of 29.6% as the specimen height decreased from 101.6 mm (H/W = 2) to 25.4 mm (H/W = 0.5) for square-shaped cross section Berea sandstone.
- The biaxial failure strength of 50.8 mm cubical specimen is 15.7% to 48.4% higher than its UCS. Therefore, both Mohr–Coulomb and Hoek–Brown failure criteria underestimate the biaxial strength of sandstone samples, as they ignore the effect of the intermediate principal stress.

Can. Geotech. J. Downloaded from cdnsciencepub.com by Indian Institute of Science Bengaluru (IISc) on 01/03/22
For personal use only.

- Generally, the biaxial strength of cubical specimen increased with the increase in intermediate principal stress (σ_2) under loading path 2. However, the peak strength dropped by 12.78% when σ_2 was kept equal to σ_1 under loading path 1, which represents high intermediate stress ($\sigma_1 = \sigma_2$).
- We analyzed peak strength under true-triaxial loading condition from two principal stress invariants: the octahedral shear stress at failure ($\tau_{oct,f}$), and the octahedral normal stress at failure ($\sigma_{oct,f}$) to consider novel loading path, i.e., $\sigma_1 = \sigma_2$ and σ_3 = constant used in the current study.
- We analyzed the transition of failure mode from uniaxial to triaxial stress conditions to understand the failure mechanism of sandstone specimens under poly-axial stress state.
- In uniaxial stress state, specimens exhibited spalling on all free faces of the cube, followed by violent failure of the mid-section. The mid-section of the specimen mostly failed in shear with multiple planes intersecting one another.
- When testing specimens biaxially, the failure mechanism exhibited varying degrees of spalling at free faces along with the shear failure of the mid-section. The intensity of spalling depended on the magnitude of confinement by the intermediate stress.
- The shear failure plane rotated with the increase in intermediate principal stress, σ_2, from plane with strike in the σ_1 direction for σ_2 = 6.9 MPa to plane with strike in the σ_2 direction for σ_2 = 27.6 MPa ($\sigma_2 = 0.45\sigma_c$). Finally, under $\sigma_1 = \sigma_2$, shear plane orientation was a combination of both σ_1 and σ_2 axis.
- In true-triaxial tests, failure was similar to biaxial tests under loading path 1 ($\sigma_1 = \sigma_2$) with splitting towards the outer surface (faces perpendicular to minimum principal stress, σ_3), and shear failure occurred in the central portion of specimen.
- The volume of specimen under splitting decreased with the increase in confinement or minimum principal stress (σ_3) from occupying a large portion of specimen at σ_3 = 0 to no splitting at σ_3 = 20.7 MPa.
- Drucker–Prager failure was initially assumed to account for the influence of intermediate principal stress (σ_2) in observed biaxial tests. However, no specific friction angle was usable for failure strength at different confining stresses.
- A regression analysis of data points at failure derived an empirical failure criterion. The criterion is a quadratic polynomial with R^2 of 0.7507.
- For true-triaxial strength envelope, 3D failure criterion by Nadai (1950) had good fit with R^2 of 0.964.

Conflict of interest statement

The authors confirm that there are no conflicts of interest associated with this publication.

Acknowledgement

Financial support for this work was provided by the Centers for Disease Control and Prevention-National Institute of Occupational Health and Safety (No. 200-2016-92214).

References

Al-Ajmi, A.M., and Zimmerman, R.W. 2005. Relation between the Mogi and the Coulomb failure criteria. International Journal of Rock Mechanics and Mining Sciences, **42**(3): 431–439. doi:10.1016/j.ijrmms.2004.11.004.

Amadei, B., Janoo, V., and Robison, M.J. 1984. Strength of Indiana limestone in true biaxial loading conditions. *In* Proceedings of the 25th U.S. Symposium on Rock Mechanics (USRMS), Evanston, Ill., 25–27 June 1984. American Rock Mechanics Association, Alexandria, Va.

Arora, S., and Mishra, B. 2015. Investigation of the failure mode of shale rocks in biaxial and triaxial compression tests. International Journal of Rock Mechanics and Mining Sciences, **79**: 109–123. doi:10.1016/j.ijrmms.2015.08.014.

ASTM. 1998. Preparing rock core specimens and determining dimensional and shape tolerances. D4543-01. *In* Annual Book of ASTM Standards. American Society of Testing and Materials. pp. 687–690.

Bétournay, M.C., and Mitri, H.S. 2003. Laboratory simulation of the behaviour of highly-stressed mining fronts. *In* Proceedings of 10th ISRM Congress, Sandton, South Africa, 8–12 September 2003.

Brown, E.T. 1974. Fracture of rock under uniform biaxial compression. *In* Proceedings of the 3rd Congress of the International Society for Rock Mechanics, Denver, Colo., 1–7 September 1974. pp. 111–117.

Cai, M. 2008. Influence of intermediate principal stress on rock fracturing and strength near excavation boundaries—insight from numerical modeling. International Journal of Rock Mechanics and Mining Sciences, **45**(5): 763–772. doi:10.1016/j.ijrmms.2007.07.026.

Colmenares, L.B., and Zoback, M.D. 2002. A statistical evaluation of intact rock failure criteria constrained by poly-axial test data for five different rocks. International Journal of Rock Mechanics and Mining Sciences, **39**(6): 695–729. doi:10.1016/S1365-1609(02)00048-5.

Drucker, D.C., and Prager, W. 1952. Soil mechanics and plastic analysis in limit design. Quarterly of Applied Mathematics, **10**: 157–165. doi:10.1090/qam/48291.

Du, K., Yang, C., Su, R., Tao, M., and Wang, S. 2020. Failure properties of cubic granite, marble, and sandstone specimens under true triaxial stress. International Journal of Rock Mechanics and Mining Sciences, **130**: 104309. doi:10.1016/j.ijrmms.2020.104309.

Feng, F., Li, X., and Li, D. 2017. Modeling of failure characteristics of rectangular hard rock influenced by sample height-to-width ratios: a finite/discrete element approach. Comptes Rendus Mécanique, **345**: 317–328. doi:10.1016/j.crme.2017.03.001.

Haimson, B., and Chang, C. 2000. A new true triaxial cell for testing mechanical properties of rock, and its use to determine rock strength and deformability of Westerly granite. International Journal of Rock Mechanics and Mining Sciences, **37**: 285–296. doi:10.1016/S1365-1609(99)00106-9.

Handin, J., Heard, H.C., and Magouirk, J.N. 1967. Effect of the intermediate principal stress on the failure of limestone, dolomite, and glass at different temperature and strain rate. Journal of Geophysical Research, **72**(2): 611–640. doi:10.1029/JZ072i002p00611.

Hobbs, D.W. 1962. The strength of coal under biaxial compression. Colliery Engineering, **39**: 285–290.

Kulatilake, P.H., Park, J., and Malama, B. 2006. A new rock mass failure criterion for biaxial loading conditions. Geotechnical and Geological Engineering, **24**(4): 871–888. doi:10.1007/s10706-005-7465-9.

Lade, P.V., and Duncan, J.M. 1975. Elastoplastic stress-strain theory for cohesionless soil. Journal of the Geotechnical Engineering Division, ASCE, **101**: 1037–1053.

Lundborg, N. 1967. The strength-size relation of granite. International Journal of Rock Mechanics and Mining Sciences & Geomechanics Abstracts, **4**(3): 269–272. doi:10.1016/0148-9062(67)90011-3.

Ma, X. 2014. Failure characteristics of compactive, porous sandstones subjected to true triaxial stresses. Ph.D. thesis, University of Wisconsin-Madison, Madison, Wisc.

Ma, X., and Haimson, B.C. 2016. Failure characteristics of two porous sandstones subjected to true triaxial stresses. Journal of Geophysical Research: Solid Earth, **121**(9): 6477–6498. doi:10.1002/2016JB012979.

Ma, X., Rudnicki, J.W., and Haimson, B.C. 2017. Failure characteristics of two porous sandstones subjected to true triaxial stresses: applied through a novel loading path. Journal of Geophysical Research: Solid Earth, **122**(4): 2525–2540. doi:10.1002/2016JB013637.

Mark, C., and Barczak, T.M. 2000. Fundamentals of coal mine roof support. *In* Proceedings: New Technology for Coal Mine Roof Support. National Institute for Occupational Safety and Health, Pittsburgh, Pa. pp. 23–42.

Matsuoka, H., and Nakai, T. 1974. Stress-deformation and strength characteristics of soil under three different principal stresses. Proceedings of the Japan Society of Civil Engineers, **1974**: 59–70. doi:10.2208/jscej1969.1974.232_59.

Mitri, H.S., Rispoli, A., and Betournay, M.C. 2005. Strength and behavior of biaxially loaded limestone rock. *In* Proceedings of Alaska Rocks 2005, The 40th U.S. Symposium on Rock Mechanics (USRMS), Anchorage, Alaska, 25–29 June 2005.

Mogi, K. 1971. Fracture and flow of rocks under high triaxial compression. Journal of Geophysical Research, **76**(5): 1255–1269. doi:10.1029/JB076i005p01255.

Nadai, A. 1950. Theory of flow and fracture of solids. McGraw-Hill, New York, NY.

Olsson, W.A. 1999. Theoretical and experimental investigation of compaction bands in porous rock. Journal of Geophysical Research: Solid Earth, **104**(B4): 7219–7228. doi:10.1029/1998JB900120.

Rudnicki, J.W. 2013. Failure of rocks in the laboratory and in the earth. *In* Proceedings of the 22nd International Congress of Theoretical and Applied Mechanics, ICTAM 2008, Adelaide, SA, Australia, 24–29 August 2008. pp. 199–215.

Smith, J.D. 1963. Condition of stress surrounding simulated mine opening. *In* Proceedings of the Rock Mechanics Symposium, Ottawa, Ont.

Walsri, C., Poonprakon, P., Thosuwan, R., and Fuenkajorn, K. 2009. Compressive and tensile strengths of sandstones under true triaxial stresses. *In* Proceedings of the 2nd Thailand Symposium on Rock Mechanics, Chonburi, Thailand, 12–13 March 2009.

Wiebols, G.A., and Cook, N.G.W. 1968. An energy criterion for the strength of rock in poly-axial compression. International Journal of Rock Mechanics and Mining Sciences & Geomechanics Abstracts, **5**(6): 529–549. doi:10.1016/0148-9062(68)90040-5.

Xu, Y.H., and Cai, M. 2017. Numerical study on the influence of cross-sectional shape on strength and deformation behaviors of rocks under uniaxial compression. Computers and Geotechnics, **84**: 129–137. doi:10.1016/j.compgeo.2016.11.017.

Yun, X.Y., Yang, X.L., and Mitri, H.S. 2008. Mechanical behavior of biaxially loaded coalmine sandstone. *In* Boundaries of Rock Mechanics: Recent Advances and Challenges for the 21st Century – Proceedings of the International Young Scholars' Symposium on Rock Mechanics, Beijing, China, 28 April–2 May 2008.

Yun, X.Y., Mitri, H.S., Yang, X.L., and Wang, Y.K. 2010. Experimental investigation into biaxial compressive strength of granite. International Journal of Rock Mechanics and Mining Sciences, **47**(2): 334–341. doi:10.1016/j.ijrmms.2009.11.004.

Can. Geotech. J. Downloaded from cdnsciencepub.com by Indian Institute of Science Bengaluru (IISc) on 01/03/22
For personal use only.